Chemical Science

ROYAL SOCIETY OF CHEMISTRY

EDGE ARTICLE

View Article Online
View Journal | View Issue

Cite this: *Chem. Sci.*, 2025, **16**, 10042

All publication charges for this article have been paid for by the Royal Society of Chemistry

Received 11th January 2025
Accepted 26th April 2025

DOI: 10.1039/d5sc00248f

rsc.li/chemical-science

Interfacial engineering of a nanofibrous Ru/Cr_2O_3 heterojunction for efficient alkaline/acid-universal hydrogen evolution at the ampere level†

Xianqiang Yu,[a] Mingze Xia,[a] Ruikai Qi,[a] Yuezhu Wang,[a] Mingbin Gao,*[b] Mengxiao Zhong*[c] and Xiaofeng Lu *[a]

Interfacial engineering of a heterostructured electrocatalyst is an efficient way to boost hydrogen production, yet it still remains a challenging task to achieve superior performance at ampere-grade current density. Herein, a nanofibrous Ru/Cr_2O_3 heterojunction is prepared for alkaline/acid-universal hydrogen evolution. Theoretical calculations reveal that the introduction of Cr_2O_3 modulates the electronic structure of Ru, which is beneficial for *H desorption, resulting in a superior HER performance at ampere-grade current density. Accordingly, the resultant Ru/Cr_2O_3 catalyst presents an ultra-low overpotential of only 88 mV and a long-term stability of 300 h at 1 A cm^{-2} in 1 M KOH. Furthermore, it also exhibits a small overpotential of 112 mV and steadily operates for 300 h at 1 A cm^{-2} in 0.5 M H_2SO_4. The catalyst outperforms not only the benchmark Pt/C catalyst but also most of the top-performing catalysts reported to date. This study offers a novel conceptual approach for designing highly efficient electrocatalysts that hold significant promise for industrial-scale water splitting applications.

Introduction

Today, environmental pollution and the energy crisis represent the most significant challenges confronting humanity.[1] Hydrogen (H_2) has the potential to emerge as a key sustainable and green energy source, given its combustion without emitting greenhouse gases, renewable nature and high gravimetric energy density.[2,3] As a vital half-reaction in water electrolysis, the hydrogen evolution reaction (HER) is widely recognized as an efficient, viable and promising route for the production of green H_2 due to its economic, clean and environmentally friendly attributes.[4–6] However, the current limitations of low efficiency, high overpotential, and the excessive reliance on the precious metal platinum (Pt) lead to prohibitively high costs for H_2 production. Additionally, many of the high-efficiency non-Pt electrocatalysts developed to date are primarily suited for low-current-density applications (less than 0.1 A cm^{-2}), rather than the high-current-density environments (1 A cm^{-2} or greater) that are essential for industrial-scale H_2 production.[7–9] Consequently, it is both challenging and crucial to design and fabricate efficient and cost-effective non-Pt HER electrocatalysts that can meet the demands of industrial H_2 production.[10–12]

As a highly promising direction in electrocatalyst research, ruthenium (Ru)-based catalysts have garnered substantial interest due to their cost-effectiveness compared to Pt and iridium (Ir), as well as their similar binding energies to Pt–H bonds.[13–15] The electronic structure of a catalyst is pivotal in determining the reaction energy barrier during catalytic processes. To modulate this structure, a variety of strategies such as vacancy engineering, doping, and interface engineering have been employed.[16–20] For instance, a hierarchical MoS_2/MoP nanorod heterojunction is constructed through a sulfuration and phosphorization process using MoO_3 nanorods as the sacrificial template for the HER.[21] The distinct hierarchical architecture of the MoS_2/MoP heterojunction facilitates electron transfer from S to P, resulting in an optimized H adsorption energy to promote the HER properties. Furthermore, the hierarchical structure provides abundant active sites and facilitates mass transfer, enabling easier H_2 release. While the creation of heterostructures significantly boosts the HER performance, it remains a formidable challenge to attain a universally high-performance catalyst that operates efficiently under both alkaline and acidic conditions at industrial-scale current densities for water splitting applications.

In this study, we successfully delineate a reliable electrospinning-calcination-thermal reduction process for constructing robust ruthenium–chromium trioxide (Ru/Cr_2O_3) heterojunction nanofibers (HNFs) as a highly efficient HER

[a]Alan G. MacDiarmid Institute, College of Chemistry, Jilin University, Changchun 130012, P. R. China. E-mail: xflu@jlu.edu.cn

[b]State Key Laboratory of Physical Chemistry of Solid Surfaces, College of Chemistry and Chemical Engineering, Xiamen University, Xiamen 361005, China. E-mail: mbgao@xmu.edu.cn

[c]State Key Laboratory of Integrated Optoelectronics, Key Laboratory of Advanced Gas Sensors, Jilin Province, College of Electronic Science and Engineering, Jilin University, Changchun, 130012, P. R. China. E-mail: zhongmx@jlu.edu.cn

† Electronic supplementary information (ESI) available. See DOI: https://doi.org/10.1039/d5sc00248f

electrocatalyst for ampere-grade-current-density water electrolysis in alkaline and acidic media. The choice of Cr_2O_3 is due to its ability to modulate the electronic structure of metals and desirable chemical stability.[22,23] In addition, the nanofibrous structure offers efficient mass transfer, which is an ideal structural system for electrocatalysis.[24–26] The resulting Ru/Cr_2O_3 HNF catalyst showcases exceptional HER activity with an ultra-low overpotential of only 88 mV and a long-term stability of 300 h at 1 A cm^{-2} in 1 M KOH. In addition, it also exhibits extremely high HER efficiency and outstanding durability in 0.5 M H_2SO_4. The excellent alkaline/acid-universal HER performances surpass that of commercial Pt/C and most documented electrocatalysts. Density functional theory (DFT) calculations reveal that the interfacial engineering in Ru/Cr_2O_3 HNFs modulates the electronic structure of Ru sites, thereby optimizing *H desorption, which yields superior HER properties in both acidic and alkaline environments.

Results and discussion

The synthetic pathway for the Ru/Cr_2O_3 HNFs is depicted in Fig. 1a, encompassing the calcination and reduction steps of the precursor nanofibers (NFs). Field emission scanning electron microscopy (FESEM) is employed to observe and scrutinize the morphological changes of NFs during the preparation process. The precursor NFs consisting of poly(vinylpyrrolidone) (PVP) and Cr^{3+}/Ru^{3+} are initially fabricated *via* an electrospinning technique, exhibiting an average diameter of approximately 453.9 nm (Fig. S1, ESI†). Following sequential calcination and reduction treatments, the mean diameter of the obtained Ru/Cr_2O_3 HNFs is reduced to be around 143.9 nm, which is caused by the thermal decomposition of the polymer within the precursor NFs under high temperature conditions (Fig. 1b and c). Moreover, the FESEM image also presents a rough surface of Ru/Cr_2O_3 HNFs, a characteristic further corroborated by the transmission electron microscopy (TEM) image (Fig. 1d). Indeed, the Ru/Cr_2O_3 HNFs are composed of a multitude of nanoparticles. The nanofibrous architecture with a similar rough surface is also observed in Ru/Cr_2O_3-1, Ru/Cr_2O_3-2 and Ru/Cr_2O_3-4 HNFs (Fig. S2, ESI†). For comparison, single metal-component R-Cr_2O_3 NFs and Ru NFs, as well as $RuCrO_x$ composite NFs, are also constructed, all demonstrating the nanofibrous morphologies (Fig. S3, ESI†). The high-resolution TEM (HRTEM) image in Fig. 1e clearly reveals the heterointerface between the (101) plane of Ru and the (110) plane of Cr_2O_3, corresponding to the lattice fringe spacings of 0.206 nm and 0.247 nm, respectively. The heterojunctions with Cr_2O_3 and Ru species may be the key factor in the highly

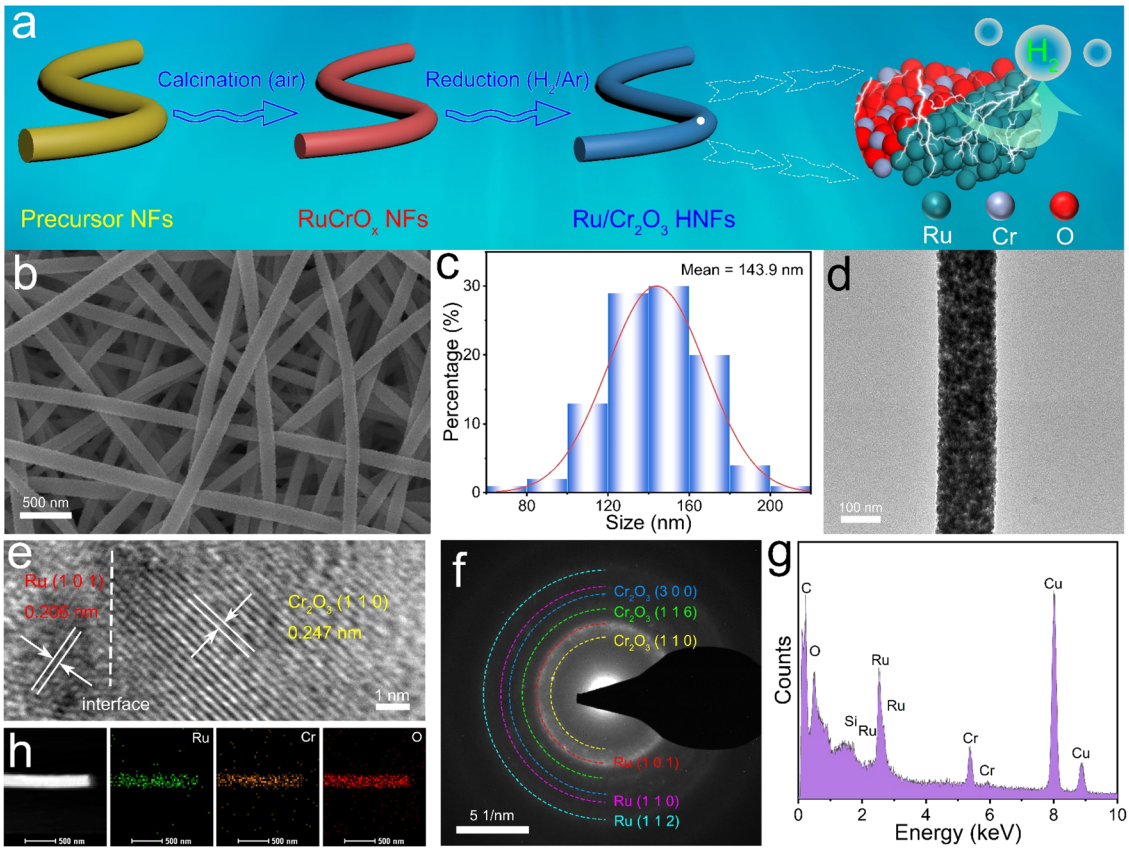

Fig. 1 (a) Schematic illustration for the synthesis of Ru/Cr_2O_3 HNFs. (b) SEM image and (c) the corresponding diameter distribution of Ru/Cr_2O_3 HNFs. (d) TEM image of a single Ru/Cr_2O_3 HNF, (e) HRTEM image of Ru/Cr_2O_3 HNFs, showing a distinct interface between Ru(101) and Cr_2O_3(110). (f) SAED pattern and (g) EDX spectrum of Ru/Cr_2O_3 HNFs. (h) HAADF-STEM image and the corresponding elemental mappings of Ru, Cr and O in Ru/Cr_2O_3 HNFs.

efficient active HER, which will be further discussed in the following investigation. The selected area electron diffraction (SAED) pattern in Fig. 1f aligns with the presence of multiple polycrystalline rings, which arises from the (101), (110) and (112) planes of Ru, and the (110), (116) and (300) planes of Cr_2O_3. Additionally, the energy-dispersive X-ray (EDX) spectroscopy analysis confirms the presence of Ru, Cr and O elements within the Ru/Cr_2O_3 HNFs (Fig. 1g). It is noted that the elemental contaminants such as C and Cu originate from the carbon-coated copper grid for TEM sample preparation, while Si is attributed to the instrument itself. The elemental mappings of Ru/Cr_2O_3 HNFs illustrate a uniform distribution of Ru, Cr and O across the entire NF structure (Fig. 1h). Furthermore, N_2 adsorption–desorption isotherms are utilized to provide the specific surface area and pore size distribution of the Ru/Cr_2O_3 HNFs (Fig. S4, ESI†). Herein, the Brunauer–Emmett–Teller (BET) surface area of Ru/Cr_2O_3 HNFs is evaluated to be 21.26 m^2 g^{-1}, and the pore size distribution is mainly dominated by mesopores.

X-ray diffraction (XRD) analysis was performed to elucidate the phase structure of the prepared Ru/Cr_2O_3 HNFs. Fig. 2a reveals that the RuO_2 NFs, characterized by the distinctive lattice planes of JCPDS No. 43-1027, are successfully reduced to form Ru NFs (JCPDS No. 06-0663) after the *in situ* H_2/argon thermal reduction process. Conversely, the Cr_2O_3 NFs retain their original crystal structure, displaying the characteristic lattice planes of Cr_2O_3 (JCPDS No. 38-1479) even after H_2/argon thermal treatment, which demonstrates no reduction occurring (Fig. 2b). In Fig. 2c, the XRD pattern of the as-synthesized $RuCrO_x$ NF sample shows the characteristic peaks of both RuO_2 and Cr_2O_3. Subsequent *in situ* H_2/argon reduction yields the Ru/Cr_2O_3 HNFs, where the XRD pattern indicates the persistence of Cr_2O_3 diffraction peaks, while the peaks associated with RuO_2 have completely vanished (Fig. 2c). In their place, the distinctive peaks of metallic Ru (JCPDS No. 06-0663) emerge, aligning with the HRTEM image findings previously discussed (Fig. 1e). Consistent outcomes are observed in the other comparative HNFs, with all diffraction peaks aligning with those of Ru (JCPDS No. 06-0663) and Cr_2O_3 (JCPDS No. 38-1479) (Fig. S5, ESI†). X-ray photoelectron spectroscopy (XPS) is further conducted to probe the surface chemical characteristics and electronic configuration of Ru/Cr_2O_3 HNFs. The survey spectrum presented in Fig. S6, ESI† confirms the presence of Ru, Cr, and O in Ru/Cr_2O_3 HNFs. Fig. 2d shows the high-resolution Ru 3p spectrum of Ru/Cr_2O_3 HNFs, which reveals two distinct doublets: the peaks positioned at 462.7 and 484.9 eV are ascribed to Ru^0 $3p_{3/2}$ and Ru^0 $3p_{1/2}$, respectively, while the weak peaks at 465.6 and 487.8 eV correspond to $Ru^{\delta+}$ $3p_{3/2}$ and $Ru^{\delta+}$ $3p_{1/2}$.[27,28] The oxidized $Ru^{\delta+}$ species may originate from exposure to air leading to surface oxidation and their interaction with the Cr_2O_3 component.[29,30] In contrast, the Ru 3p XPS spectrum of $RuCrO_x$ NFs shows a pair of strong peaks located at 463.6 and 485.9 eV, attributable to Ru^{4+} (Fig. S7, ESI†).[31] In the Cr 2p spectrum of Ru/Cr_2O_3 HNFs (Fig. 2e), the prominent characteristic peaks observed at binding energies of 576.9 and 587.0 eV are attributed to Cr^{3+} $2p_{3/2}$ and Cr^{3+} $2p_{1/2}$, respectively.[22,32,33] In addition, the narrow-scan O 1s spectrum reveals two distinct components with binding energies at 530.7 and 532.1 eV (Fig. 2f), which correspond to lattice oxygen and adsorbed oxygen species, respectively.[34–36] These findings collectively provide compelling evidence that Ru/Cr_2O_3 HNFs have been successfully synthesized.

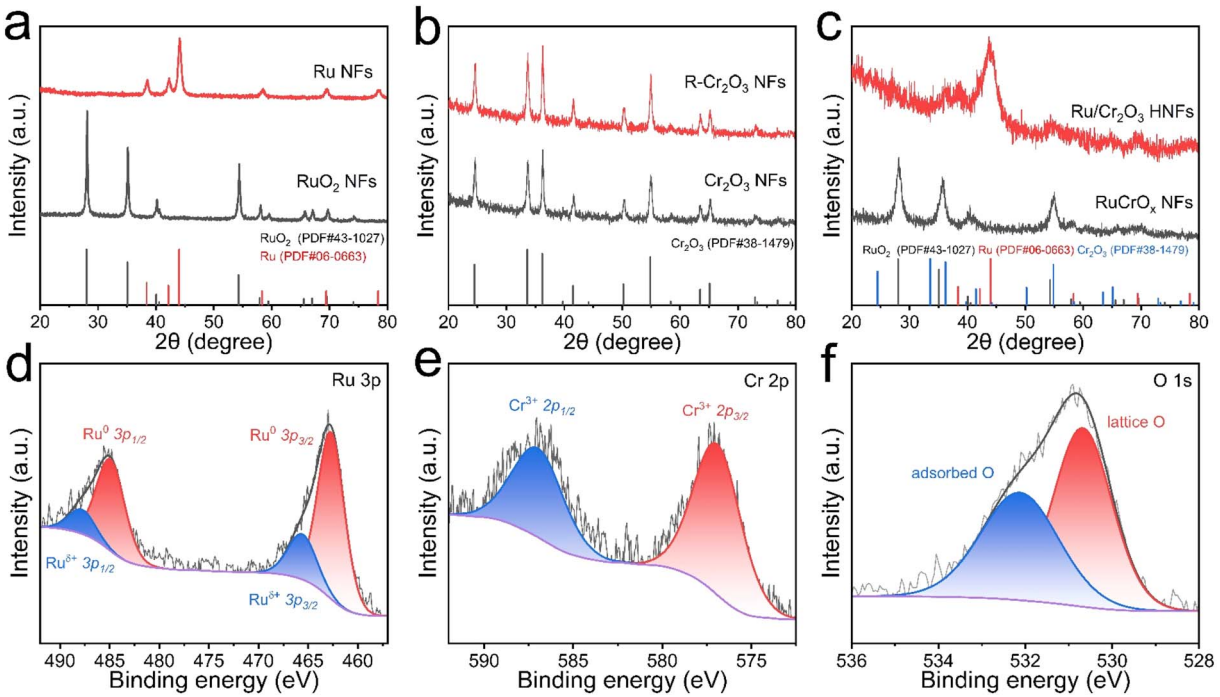

Fig. 2 XRD patterns of (a) RuO_2 NFs and Ru NFs, (b) Cr_2O_3 NFs and R-Cr_2O_3 NFs, and (c) $RuCrO_x$ NFs and Ru/Cr_2O_3 HNFs. Typical high-resolution (d) Ru 3p, (e) Cr 2p and (f) O 1s XPS spectra of Ru/Cr_2O_3 HNFs.

Initially, the HER properties of the synthesized Ru/Cr_2O_3 HNFs are examined in 1 M KOH. Furthermore, to provide a benchmark, the HER activities of commercial 20% Pt/C and other nanofibrous catalysts prepared using varied experimental parameters are assessed for comparison. Fig. 3a and S8, ESI† present the linear sweep voltammetry (LSV) curves along with the corresponding overpotentials required to reach current densities of 0.1 and 1 A cm^{-2} for Ru/Cr_2O_3 HNFs, R-Cr_2O_3 NFs, $RuCrO_x$ NFs, Ru NFs and commercial 20% Pt/C. Ru/Cr_2O_3 HNFs exhibit an overpotential of merely 41 mV at 0.1 A cm^{-2}, significantly outperforming the R-Cr_2O_3 NFs with negligible HER activity, as well as $RuCrO_x$ NFs (135 mV), Ru NFs (88 mV) and 20% Pt/C catalyst (87 mV), respectively. Notably, the prepared Ru-based catalysts exhibit more favorable HER performances compared to the R-Cr_2O_3 NF sample, which illustrates the key role of Ru species in the heterojunctions. Afterwards, the Ru/Cr_2O_3 HNF catalyst is optimized by controlling the molar ratio between Ru and Cr in the spinning solution. As illustrated in Fig. S9, ESI,† the optimized Ru/Cr_2O_3 HNFs with the Ru : Cr molar ratio of 3 : 1 demonstrate superior HER activity compared to the other comparative HNFs. Moreover, the mass activity (MA_{Ru}) values are calculated to evaluate the practical viability and cost-effectiveness of the catalysts. As anticipated, Ru/Cr_2O_3 HNFs boast the highest MA_{Ru} value of 1536.11 A g_{Ru}^{-1} at the overpotential of 100 mV, much better than other control catalysts, including Ru/Cr_2O_3-1 HNFs (898.62 A g_{Ru}^{-1}), Ru/Cr_2O_3-2 HNFs (1220.54 A g_{Ru}^{-1}), Ru/Cr_2O_3-4 HNFs (812.48 A g_{Ru}^{-1}), Ru NFs (129.89 A g_{Ru}^{-1}), and $RuCrO_x$ NFs (48.73 A g_{Ru}^{-1}) (Fig. S10a, ESI†). After that, turnover frequency (TOF) values are calculated to delve into the intrinsic HER activity of catalysts. The highest TOF value of 0.604 s^{-1} at the overpotential of 100 mV is achieved by Ru/Cr_2O_3 HNFs, which is also markedly superior to other control catalysts (Fig. S10b, ESI†). It is worth noting that all the prepared HNF samples possess much higher MA_{Ru} and TOF values than single component Ru NFs and unreduced $RuCrO_x$ NF catalysts, further revealing the highly efficient active sites in the heterojunctions of Ru/Cr_2O_3 during the alkaline HER.

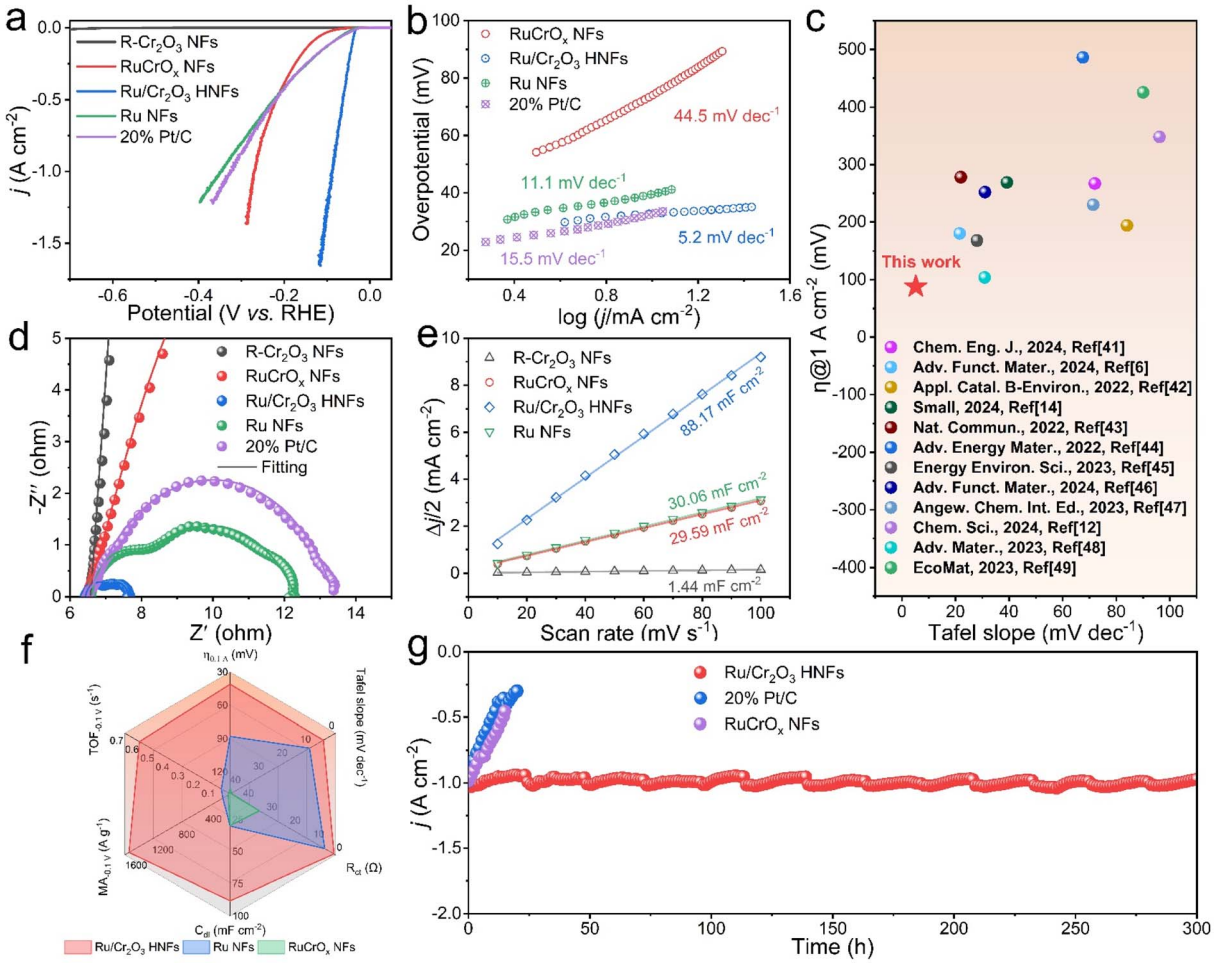

Fig. 3 HER performance of Ru/Cr_2O_3 HNFs and other catalysts in 1 M KOH. (a) LSV curves of different catalysts including Ru/Cr_2O_3 HNFs, R-Cr_2O_3 NFs, $RuCrO_x$ NFs, Ru NFs and 20% Pt/C. (b) Tafel plots of Ru/Cr_2O_3 HNFs, $RuCrO_x$ NFs, Ru NFs and 20% Pt/C. (c) Comparison of overpotentials at 1 A cm^{-2} with Tafel slopes in diverse HER electrocatalysts. (d) Nyquist plots and fitting curves at −1.0 V *versus* the Hg/HgO electrode for the HER. (e) The relationship between half of the capacitive current density and the scan rates to yield C_{dl} values. (f) Comparison of the overpotential at 0.1 A cm^{-2}, Tafel slope, R_{ct}, C_{dl}, MA and TOF of Ru/Cr_2O_3 HNFs, Ru NFs, and $RuCrO_x$ NFs. (g) The *i*–*t* curves of Ru/Cr_2O_3 HNFs, $RuCrO_x$ NFs and commercial Pt/C catalyst at a current density of ≈1 A cm^{-2}.

The Tafel slope of Ru/Cr_2O_3 HNFs (5.2 mV dec^{-1}) is also notably lower than those of $RuCrO_x$ NFs (44.5 mV dec^{-1}), Ru NFs (11.1 mV dec^{-1}) and the commercial 20% Pt/C catalyst (15.5 mV dec^{-1}), suggesting the Volmer–Tafel mechanism as the HER pathway[37,38] and signifying the exceptional catalytic kinetics of Ru/Cr_2O_3 NFs (Fig. 3b). The ability to achieve high catalytic activity at industrial-grade current density is essential for the practical application of electrocatalysts.[39,40] Remarkably, the Ru/Cr_2O_3 HNFs require an overpotential of only 88 mV to attain a current density of 1 A cm^{-2} in 1 M KOH, which is also significantly better than the other comparative catalysts (Fig. S8 and S9, ESI†). Owing to the ultra-low overpotential at ampere-grade current density and Tafel slope, Ru/Cr_2O_3 HNFs exhibit the most outstanding HER activity among the recently reported high-current-density HER catalysts in alkaline environments (Fig. 3c and Table S1, ESI†).[6,12,14,41–49] Subsequently, to elucidate the origin of the high catalytic activity of Ru/Cr_2O_3 HNFs in alkaline environments, electrochemical impedance spectroscopy (EIS) analysis is conducted to assess the interfacial charge transfer capability. The Nyquist plots obtained at the potential of −1.0 V *vs.* the Hg/HgO electrode, as depicted in Fig. 3d, reveal that the charge transfer resistance (R_{ct}) value of Ru/Cr_2O_3 HNFs (0.67 Ω) is much lower than those of commercial Pt/C (6.77 Ω), $RuCrO_x$ NFs (32.56 Ω), Ru NFs (4.64 Ω), and R-Cr_2O_3 NFs (10 230 Ω), indicating a substantial enhancement in charge transfer capacity for the heterostructure, which contributes to the enhanced HER efficiency. The equivalent circuit model used for fitting the EIS data is presented in Fig. S11, ESI.†

The double-layer capacitance (C_{dl}) values for different catalysts are determined from cyclic voltammetry (CV) curves obtained in the non-Faraday potential region, which correlates positively with the electrochemical active surface area (ECSA) (Fig. S12 and S13, ESI†).[50] The ECSA values reflect the number of active sites available for the electrocatalytic process.[51,52] The C_{dl} value of the Ru/Cr_2O_3 HNFs is 88.17 mF cm^{-2}, which is approximately 61.23, 2.98, and 2.93 times as high as that of R-Cr_2O_3 NFs, $RuCrO_x$ NFs and Ru NFs, respectively (Fig. 3e). Evidently, the Ru/Cr_2O_3 HNFs possess a higher estimated ECSA and roughness factor (RF) values of 198.38 cm^2 and 2204, respectively, compared to the other comparative catalysts (Table S2, ESI†). Based on these ECSA values, the ECSA-normalized LSVs are employed to gauge their intrinsic activity (Fig. S14a, ESI†). And as expected, Ru/Cr_2O_3 HNFs show the lowest overpotential of 91 mV at a current density of 0.5 mA cm_{ECSA}^{-2} compared to that of $RuCrO_x$ NFs and Ru NFs (Fig. S14b, ESI†). This demonstrates that the heterostructure not only effectively exposes a great number of HER active sites, but also significantly increases the activity of each site. Fig. 3f shows the six pivotal factors for HER catalysts. It is readily apparent that the Ru/Cr_2O_3 HNFs encompass the largest area in each category compared to the $RuCrO_x$ NFs and Ru NFs, signifying their exceptional electrocatalytic performance in the HER process.

Beyond the exploration into electrocatalytic activity, the stability test is also a crucial factor in evaluating the viability of a catalyst for real-world application. Remarkably, the Ru/Cr_2O_3 HNFs work stably at a high current density of 1 A cm^{-2}, retaining over 90% of the initial current density even after 300 h of continuous operation in an alkaline medium, as evidenced by the *i*–*t* test (Fig. 3g). Obviously, the stability of Ru/Cr_2O_3 HNFs is considerably better than that of $RuCrO_x$ NFs (45% after 15 h) and commercial Pt/C catalyst (30% after 20 h). To shed light on the structural stability of Ru/Cr_2O_3 HNFs throughout the HER process, a comprehensive suite of characterization studies was conducted after the *i*–*t* testing. Fig. S15, ESI† shows the SEM image of the Ru/Cr_2O_3 HNF catalyst post HER, illustrating its morphological and structural robustness. Moreover, the XRD spectra of the catalyst exhibit no discernible phase transformation, thereby realizing the stability of the crystal structure of the Ru/Cr_2O_3 HNFs (Fig. S16a, ESI†). The surface chemical valence states of the catalyst following the HER process are further probed in greater detail using XPS spectroscopy (Fig. S16b–d, ESI†). A comparison of the Ru 3p, Cr 2p and O 1s spectra of the Ru/Cr_2O_3 HNFs before and after the HER test indicates that there are no substantial alterations, underscoring the stability of the catalyst. Furthermore, the electrolyte for Ru/Cr_2O_3 HNFs after 300 h of continuous HER stability test in 1 M KOH was examined by inductively coupled plasma-optical emission spectrometry (ICP-OES) to estimate the dissolved amount of Ru. The results show that only a very small amount (1.7 wt%) of Ru is dissolved in the electrolyte during the HER stability test, indicating the excellent stability of Ru/Cr_2O_3 HNFs under alkaline conditions.

The HER performance of these samples in acidic media (0.5 M H_2SO_4) is also evaluated using a standard three-electrode system. As depicted in Fig. 4a and S17, ESI,† the Ru/Cr_2O_3 HNFs still retain high catalytic activity, requiring a mere overpotential of 35 mV to reach a current density of 0.1 A cm^{-2}. Notably, this overpotential is not only significantly lower than those of $RuCrO_x$ NFs (179 mV) and Ru NFs (176 mV), but also smaller than that of commercial Pt/C (41 mV). Similarly, the Ru/Cr_2O_3 HNFs also demonstrate the best HER activity in acidic media when compared to the samples obtained under other experimental conditions (Fig. S18, ESI†). In addition, in 0.5 M H_2SO_4, the Ru/Cr_2O_3 HNFs achieve the highest MA_{Ru} value of 900.28 A g_{Ru}^{-1} at an overpotential of 100 mV, far surpassing the performance of the other control catalysts (Fig. S19a, ESI†). The Ru/Cr_2O_3 HNFs also attain the highest TOF value of 0.354 s^{-1} at an overpotential of 100 mV in 0.5 M H_2SO_4, which is significantly superior to that of other control catalysts (Fig. S19b, ESI†). Additionally, the Ru/Cr_2O_3 HNFs achieve a remarkable current density of 1 A cm^{-2} with a reduced overpotential of just 112 mV, outperforming the other control catalysts and highlighting their exceptional HER activity for practical application (Fig. S17 and S18b, ESI†). The corresponding Tafel slopes of Ru/Cr_2O_3 HNFs, commercial Pt/C, $RuCrO_x$ NFs, and Ru NFs are 33.4, 38.3, 65.9, and 83.5 mV dec^{-1}, respectively (Fig. 4b). These findings also suggest that the heterostructure of Ru and Cr_2O_3 can markedly promote the HER reaction kinetics in acidic environments. Fortunately, the robust catalytic activity of Ru/Cr_2O_3 HNFs in 0.5 M H_2SO_4 is on par with or even exceeds the performance of recently reported top-tier electrocatalysts (Fig. 4c and Table S3, ESI†).[44,53–64] Furthermore, EIS measurement reveals that the Ru/Cr_2O_3 HNFs exhibit an exceptionally low R_{ct} of merely 2.0 Ω, which is far below than that of the other catalysts (Fig. 4d and

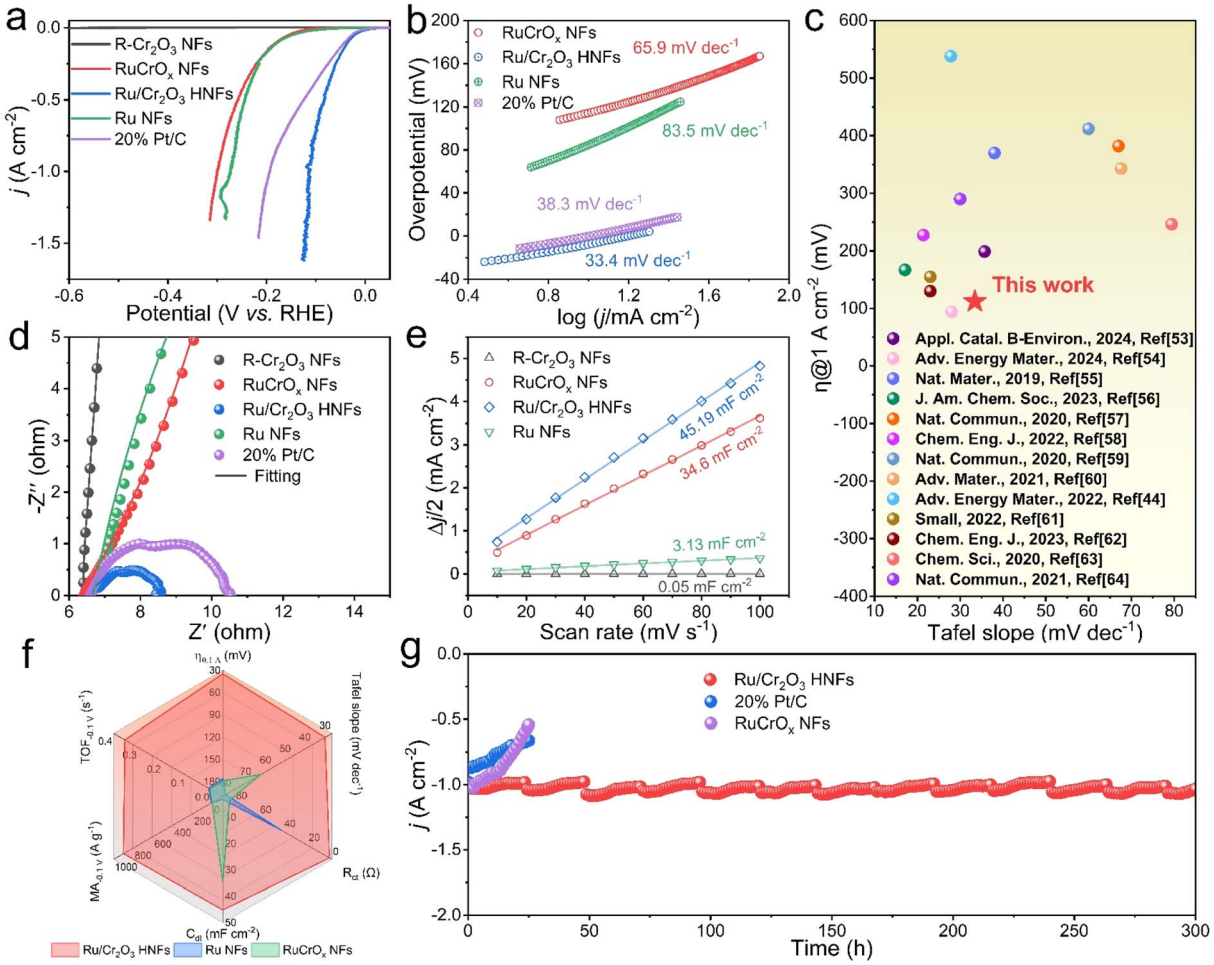

Fig. 4 HER performance of Ru/Cr_2O_3 HNFs and other catalysts in 0.5 M H_2SO_4. (a) LSV curves of different catalysts including Ru/Cr_2O_3 HNFs, R-Cr_2O_3 NFs, $RuCrO_x$ NFs, Ru NFs and 20% Pt/C. (b) Tafel plots of Ru/Cr_2O_3 HNFs, $RuCrO_x$ NFs, Ru NFs and 20% Pt/C. (c) Comparison of overpotentials at 1 A cm^{-2} with Tafel slopes in diverse HER electrocatalysts. (d) Nyquist plots and fitting curves at −0.3 V *versus* the Ag/AgCl electrode for the HER. (e) The relationship between half of the difference in current density and the scan rates to yield C_{dl} values. (f) Comparison of the overpotential at 0.1 A cm^{-2}, Tafel slope, R_{ct}, C_{dl}, MA and TOF of Ru/Cr_2O_3 HNFs, Ru NFs, and $RuCrO_x$ NFs. (g) The *i*–*t* curves of Ru/Cr_2O_3 HNFs, $RuCrO_x$ NFs and commercial Pt/C catalyst at a current density of ≈1 A cm^{-2}.

S18c, ESI†). This low R_{ct} value suggests an enhanced electrical conductivity and efficient electron transfer capability within the Ru/Cr_2O_3 HNFs, beneficial for promoting the HER activity.[9,65] The ECSA values of these electrocatalysts are estimated by assessing the directly related C_{dl} values (Fig. S20 and S21, ESI†). As illustrated in Fig. 4e, the calculated C_{dl} value for Ru/Cr_2O_3 HNFs is 45.19 mF cm^{-2}, which exceeds that of $RuCrO_x$ NFs (34.6 mF cm^{-2}) and is substantially greater than those of the Ru NFs (3.13 mF cm^{-2}) and R-Cr_2O_3 NFs (0.05 mF cm^{-2}). Clearly, the Ru/Cr_2O_3 HNFs also possess a higher estimated ECSA and RF values of 101.68 cm^2 and 1130, respectively, compared to other catalysts in acidic environments (Table S4, ESI†). In addition, ECSA normalization is also performed to evaluate the intrinsic activity of synthesized catalysts under acidic conditions (Fig. S22, ESI†). The results show that Ru/Cr_2O_3 HNFs exhibit a low overpotential of only 92 mV at 0.5 mA cm_{ECSA}^{-2}, which is much better than that of $RuCrO_x$ NFs (249 mV) and Ru NFs (137 mV), indicating that Ru/Cr_2O_3 HNFs possess both a larger ECSA and higher intrinsic activity.

Further, the radargram presented in Fig. 4f demonstrates that Ru/Cr_2O_3 HNFs exhibit an outstanding electrocatalytic performance compared to $RuCrO_x$ NFs and Ru NFs for the acidic HER, suggesting the exceptional advantage of the heterojunction construction of metallic Ru and Cr_2O_3 in the acidic HER process. Additionally, Ru/Cr_2O_3 HNFs also showcase exceptional durability in catalyzing acidic HER. In a continuous *i*–*t* test conducted in 0.5 M H_2SO_4 with a constant applied potential, Ru/Cr_2O_3 HNFs sustain up to 300 h of HER progression at a high current density of 1 A cm^{-2}, retaining a stable current density (Fig. 4g). In contrast, both $RuCrO_x$ NFs and the commercial Pt/C catalyst decay rapidly within 25 h, further confirming the superior long-term stability of the Ru/Cr_2O_3 HNFs. Finally, we have examined the surface structure and chemical compositions of the Ru/Cr_2O_3 NFs after the acidic HER stability test. The SEM image (Fig. S23, ESI†) and XRD pattern (Fig. S24a, ESI†) exhibit no significant alterations in either morphology or crystal structure. The surface chemical valence states of the catalyst after the acidic HER process is

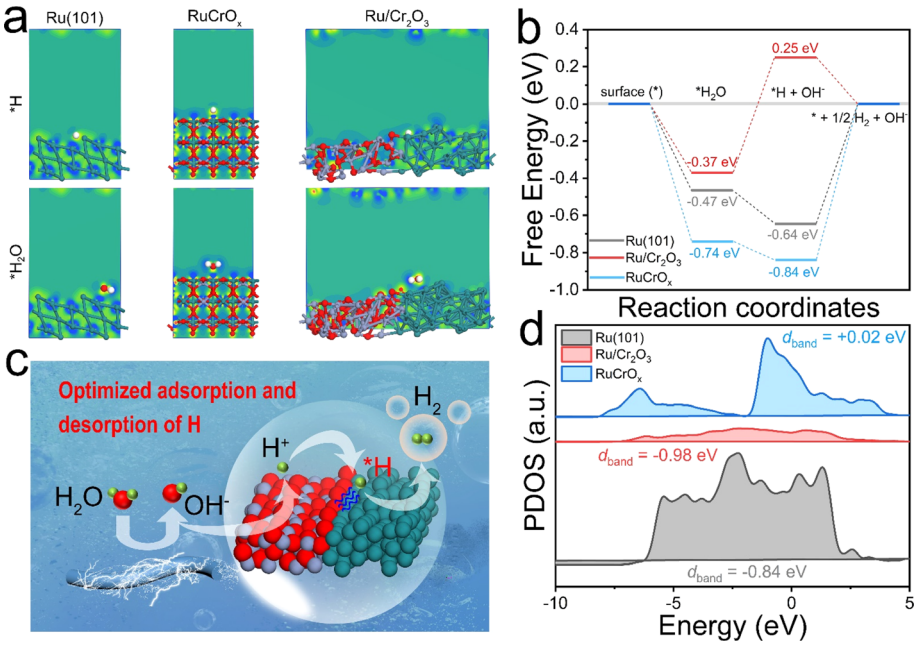

Fig. 5 (a) The charge differential density maps of the adsorption of *H and *H_2O on Ru(101), $RuCrO_x$ and Ru/Cr_2O_3 models, where blue and yellow represent electron density decrease and increase, respectively. The green, cyan and red spheres represent Ru, Cr and O atoms, respectively. (b) Calculated adsorption energies of *H_2O and *H on the surface for Ru(101), $RuCrO_x$ and Ru/Cr_2O_3 models. (c) Schematic illustration of the proposed HER catalytic mechanism on Ru/Cr_2O_3 HNFs. (d) The PDOS of Ru atoms for Ru(101), $RuCrO_x$ and Ru/Cr_2O_3 models.

further investigated using XPS spectroscopy (Fig. S24b–d, ESI†). Compared with the Ru 3p, Cr 2p and O 1s spectra of Ru/Cr_2O_3 NFs before the HER test, no substantial differences are observed, demonstrating the compositional stability of the catalyst during the acidic HER process.

To delve into the origin of the high activity on Ru/Cr_2O_3, periodic density functional theory (DFT) calculations are conducted. The structural models are constructed including Ru(101), $RuCrO_x$ and Ru/Cr_2O_3 (Fig. S25, ESI†). Fig. 5a displays the schematic diagram of the adsorption of *H_2O and *H on three different models.[66–68] The kinetic energy for H_2O adsorption (ΔG (*H_2O)), hydrogen adsorption (ΔG (*H)), and final H_2 release is calculated based on the optimized models for Ru/Cr_2O_3, Ru(101) and $RuCrO_x$. The adsorption energies of ΔG (*H_2O) and ΔG (*H) have been widely accepted as descriptors to evaluate the HER activity of catalysts. In Fig. 5b, the adsorption of H_2O occurs almost spontaneously on all three models since the ΔG (*H_2O) is less than 0. The value of ΔG (*H) close to 0 eV is considered to be ideal for the HER.[7,69] It can be found that the value of ΔG (*H) for Ru/Cr_2O_3 is |0.25 eV|, which is much closer to 0 eV than the corresponding values for Ru(101) (|−0.64 eV|) and $RuCrO_x$ (|−0.84 eV|). This indicates that the interface of the Ru site in proximity to the Cr_2O_3 possesses the most favorable *H adsorption kinetics. Moreover, the hydrogen evolution process is exergonic on the surface of Ru/Cr_2O_3 while it is thermodynamically uphill on the surface of the other two models, indicating that the construction of the Ru/Cr_2O_3 heterojunction interface facilitates *H desorption and thus accelerates the release of H_2. The possible reason for this phenomenon is that the Cr_2O_3 surface effectively modulates the electronic properties of Ru, thereby optimizing the adsorption and desorption of *H (Fig. 5c). This leads to superior HER performance in both alkaline and acidic environments, which can be further substantiated by examining the projected density of states (PDOS). As depicted in Fig. 5d, the d-band centers of Ru in the Ru/Cr_2O_3, Ru(101) and $RuCrO_x$ models relative to the Fermi level are calculated to be −0.98, −0.84 and +0.02 eV, respectively, illustrating that the d-band center is far away from the Fermi level at the heterojunction interface between Ru and Cr_2O_3. This downshift suggests a weakened interaction between *H and the Ru active site at the heterojunction interface,[67] which facilitates the H_2 release from the heterojunction interface of Ru/Cr_2O_3. Furthermore, the differential charge density maps visualize the interaction between *H, *H_2O and the surface of catalyst models (Fig. 5a). The robust interactions between *H and Ru in $RuCrO_x$ lead to a strong adsorption of *H on $RuCrO_x$, resulting in the higher desorption energy of *H on $RuCrO_x$. Conversely, the weak interactions between *H and Ru in Ru/Cr_2O_3 facilitate *H desorption, thereby lowering the energy barrier for the HER. The above analysis underscores that the synergistic interaction between Ru and Cr_2O_3 enhances the electrocatalytic performance of Ru/Cr_2O_3 HNFs for the HER.

Conclusion

In summary, we have successfully fabricated a nanofibrous Ru/Cr_2O_3 heterojunction through an electrospinning-calcination-thermal reduction procedure for efficient alkaline/acid-universal electrocatalytic properties at industrial-grade current density. The obtained Ru/Cr_2O_3 HNF catalyst achieves an exceptional HER activity and long-term stability at a high current density of 1 A cm^{-2}, significantly outperforming

commercial Pt/C and many recently reported top-tier electrocatalysts. DFT calculations reveal that the construction of the heterojunction of Ru/Cr_2O_3 optimizes the *H desorption capability during the HER process. In addition, the strong interactions between Ru and Cr_2O_3 enable more charge carriers participating in the electrocatalytic reactions, resulting in a promoted HER performance. This approach of significantly enhancing the alkaline/acid-universal HER properties at the ampere level can be broadened as a novel design paradigm for other catalyst systems, thereby advancing the evolution and practical utilization for high-efficiency H_2 production.

Data availability

The data supporting this article have been included as part of the ESI.†

Author contributions

X. Lu, M. Zhong and M. Gao supervised this project. X. Yu performed the experiments and characterized the catalysts. X. Yu, M. Xia, R. Qi, Y. Wang and M. Zhong analyzed the data. M. Gao carried out the theoretical calculation. X. Yu and M. Gao wrote the manuscript. X. Lu and M. Zhong revised the manuscript. All authors have approved the final version of the manuscript.

Conflicts of interest

The authors declare no conflict of interest.

Acknowledgements

This work was financially supported by the National Natural Science Foundation of China (52273056 and 22208337) and the Jilin Province Science and Technology Development Program (YDZJ202501ZYTS305).

References

1 S. Chu and A. Majumdar, *Nature*, 2012, **488**, 294–303.
2 M. D. Allendorf, V. Stavila, J. L. Snider, M. Witman, M. E. Bowden, K. Brooks, B. L. Tran and T. Autrey, *Nat. Chem.*, 2022, **14**, 1214–1223.
3 R.-T. Liu, Z.-L. Xu, F.-M. Li, F.-Y. Chen, J.-Y. Yu, Y. Yan, Y. Chen and B. Y. Xia, *Chem. Soc. Rev.*, 2023, **52**, 5652–5683.
4 Y. Jiang, Z. Liang, H. Fu, M. Sun, S. Wang, B. Huang and Y. Du, *J. Am. Chem. Soc.*, 2024, **146**, 9012–9025.
5 Y.-C. Zhang, M. Zhao, J. Wu, Y. Wang, L. Zheng, F. Gu, J.-J. Zou, J. Gao and X.-D. Zhu, *ACS Catal.*, 2024, **14**, 7867–7876.
6 J. Liu, J. Ren, Y. Du, X. Chen, M. Wang, Y. Liu and L. Wang, *Adv. Funct. Mater.*, 2024, **34**, 2315773.
7 L. Zhang, H. Hu, C. Sun, D. Xiao, H.-T. Wang, Y. Xiao, S. Zhao, K. H. Chen, W.-X. Lin, Y.-C. Shao, X. Wang, C.-W. Pao and L. Han, *Nat. Commun.*, 2024, **15**, 7179.
8 Q. Hu, J. Cao, S. Qi, N. Meng, J. Zhao, T. Huang, J. You, T. Liang, C. Shang, J. Yu, H. Yang and C. He, *Angew. Chem., Int. Ed.*, 2024, e202416402.
9 J.-B. Chen, J. Ying, Y.-X. Xiao, G. Tian, Y. Dong, L. Shen, S. I. Córdoba de Torresi, M. D. Symes, C. Janiak and X.-Y. Yang, *ACS Catal.*, 2023, **13**, 14802–14812.
10 W. Li, C. Wang and X. Lu, *J. Mater. Chem. A*, 2021, **9**, 3786–3827.
11 L. Zhang, W. Li, S. Ren, W. Song, C. Wang and X. Lu, *Adv. Energy Mater.*, 2024, 2403136.
12 W. Li, W. Gou, L. Zhang, M. Zhong, S. Ren, G. Yu, C. Wang, W. Chen and X. Lu, *Chem. Sci.*, 2024, **15**, 11890–11901.
13 D. Wu, K. Kusada, S. Yoshioka, T. Yamamoto, T. Toriyama, S. Matsumura, Y. Chen, O. Seo, J. Kim, C. Song, S. Hiroi, O. Sakata, T. Ina, S. Kawaguchi, Y. Kubota, H. Kobayashi and H. Kitagawa, *Nat. Commun.*, 2021, **12**, 1145.
14 W. Li, R. Liu, G. Yu, X. Chen, S. Yan, S. Ren, J. Chen, W. Chen, C. Wang and X. Lu, *Small*, 2024, **20**, 2307164.
15 M. Li, H. Wang, W. Zhu, W. Li, C. Wang and X. Lu, *Adv. Sci.*, 2020, **7**, 1901833.
16 C. W. Lee, C. Cazorla, S. Zhou, D. Zhang, H. Xu, W. Zhong, M. Zhang, D. Chu, Z. Han and R. Amal, *Adv. Energy Mater.*, 2024, 2402786.
17 B. Zhang, J. Wang, G. Liu, C. M. Weiss, D. Liu, Y. Chen, L. Xia, P. Zhou, M. Gao, Y. Liu, J. Chen, Y. Yan, M. Shao, H. Pan and W. Sun, *Nat. Catal.*, 2024, **7**, 441–451.
18 J. Li, X. Meng, X. Song, J. Qi, F. Liu, X. Xiao, Y. Du, G. Xu, Z. Jiang, S. Ye, S. Huang and J. Qiu, *Adv. Funct. Mater.*, 2024, **34**, 2316718.
19 S. Zuo, Z.-P. Wu, D. Xu, R. Ahmad, L. Zheng, J. Zhang, L. Zhao, W. Huang, H. Al Qahtani, Y. Han, L. Cavallo and H. Zhang, *Nat. Commun.*, 2024, **15**, 9514.
20 M. Li, X. Wang, K. Liu, H. Sun, D. Sun, K. Huang, Y. Tang, W. Xing, H. Li and G. Fu, *Adv. Mater.*, 2023, **35**, 2302462.
21 Q. Liu, Z. Xue, B. Jia, Q. Liu, K. Liu, Y. Lin, M. Liu, Y. Li and G. Li, *Small*, 2020, **16**, 2002482.
22 H. Q. Fu, J. Liu, N. M. Bedford, Y. Wang, J. W. Sun, Y. Zou, M. Dong, J. Wright, H. Diao, P. Liu, H. G. Yang and H. Zhao, *Adv. Mater.*, 2022, **34**, 2202854.
23 M. Gong, W. Zhou, M. J. Kenney, R. Kapusta, S. Cowley, Y. Wu, B. Lu, M.-C. Lin, D.-Y. Wang, J. Yang, B.-J. Hwang and H. Dai, *Angew. Chem., Int. Ed.*, 2015, **54**, 11989–11993.
24 W. Li, L. Zhang, L. Ma, J. Wang, R. Qi, Y. Pang, M. Xu, C. Zhao, C. Wang, M. Gao and X. Lu, *Nano Lett.*, 2025, **25**, 443–452.
25 Y. Wang, X. Yu, J. Xu, M. Zhong, J. Hao, M. Gao and X. Lu, *Chem. Eng. J.*, 2025, **505**, 159561.
26 S. Liu, K. Ma, H. Teng, W. Miao, X. Zhou, X. Cui, X. Zhou, L. Jiang and S. Guo, *Adv. Mater.*, 2025, **37**, 2411148.
27 H. Yao, X. Wang, K. Li, C. Li, C. Zhang, J. Zhou, Z. Cao, H. Wang, M. Gu, M. Huang and H. Jiang, *Appl. Catal., B*, 2022, **312**, 121378.
28 Q. He, Y. Zhou, H. Shou, X. Wang, P. Zhang, W. Xu, S. Qiao, C. Wu, H. Liu, D. Liu, S. Chen, R. Long, Z. Qi, X. Wu and L. Song, *Adv. Mater.*, 2022, **34**, 2110604.
29 F. Yang, Y. Zhao, Y. Du, Y. Chen, G. Cheng, S. Chen and W. Luo, *Adv. Energy Mater.*, 2018, **8**, 1703489.

30 C. Hu, E. Song, M. Wang, W. Chen, F. Huang, Z. Feng, J. Liu and J. Wang, *Adv. Sci.*, 2021, **8**, 2001881.
31 X. Miao, Z. Peng, L. Shi and S. Zhou, *ACS Catal.*, 2023, **13**, 3983–3989.
32 J. Guo, Y. Zheng, Z. Hu, C. Zheng, J. Mao, K. Du, M. Jaroniec, S.-Z. Qiao and T. Ling, *Nat. Energy*, 2023, **8**, 264–272.
33 S. Li, T. Liu, W. Zhang, M. Wang, H. Zhang, C. Qin, L. Zhang, Y. Chen, S. Jiang, D. Liu, X. Liu, H. Wang, Q. Luo, T. Ding and T. Yao, *Nat. Commun.*, 2024, **15**, 3416.
34 L. Wang, Y. Zhu, Y. Wen, S. Li, C. Cui, F. Ni, Y. Liu, H. Lin, Y. Li, H. Peng and B. Zhang, *Angew. Chem., Int. Ed.*, 2021, **60**, 10577–10582.
35 J. Zheng, D. Meng, J. Guo, X. Liu, L. Zhou and Z. Wang, *Adv. Mater.*, 2024, **36**, 2405129.
36 P. Xue, M. Qiao, J. Miao, Y. Tang, D. Zhu and C. Guo, *Chem. Commun.*, 2024, **60**, 6423–6426.
37 J. Mahmood, F. Li, S.-M. Jung, M. S. Okyay, I. Ahmad, S.-J. Kim, N. Park, H. Y. Jeong and J.-B. Baek, *Nat. Nanotechnol.*, 2017, **12**, 441–446.
38 P. Su, W. Pei, X. Wang, Y. Ma, Q. Jiang, J. Liang, S. Zhou, J. Zhao, J. Liu and G. Q. Lu, *Angew. Chem., Int. Ed.*, 2021, **60**, 16044–16050.
39 Y. Luo, Z. Zhang, M. Chhowalla and B. Liu, *Adv. Mater.*, 2022, **34**, 2108133.
40 A. A. Feidenhans'l, Y. N. Regmi, C. Wei, D. Xia, J. Kibsgaard and L. A. King, *Chem. Rev.*, 2024, **124**, 5617–5667.
41 B. Wang, H. Sun, M. Chen, T. Zhou, H. Zheng, M. Zhang, B. Xiao, J. Zhao, Y. Zhang, J. Zhang and Q. Liu, *Chem. Eng. J.*, 2024, **479**, 147500.
42 Y.-N. Zhou, F.-L. Wang, J. Nan, B. Dong, H.-Y. Zhao, F.-G. Wang, N. Yu, R.-N. Luan, D.-P. Liu and Y.-M. Chai, *Appl. Catal., B*, 2022, **304**, 120917.
43 Y. Zhang, K. E. Arpino, Q. Yang, N. Kikugawa, D. A. Sokolov, C. W. Hicks, J. Liu, C. Felser and G. Li, *Nat. Commun.*, 2022, **13**, 7784.
44 G. Zhang, A. Wang, L. Niu, W. Gao, W. Hu, Z. Liu, R. Wang and J. Chen, *Adv. Energy Mater.*, 2022, **12**, 2103511.
45 L. Gao, F. Bao, X. Tan, M. Li, Z. Shen, X. Chen, Z. Tang, W. Lai, Y. Lu, P. Huang, C. Ma, S. C. Smith, Z. Ye, Z. Hu and H. Huang, *Energy Environ. Sci.*, 2023, **16**, 285–294.
46 Y. Huang, X. Zhang, L. Li, M. Humayun, H. Zhang, X. Xu, S. P. Anthony, Z. Chen, J. Zeng, D. V. Shtansky, K. Huo, H. Song, C. Wang and W. Zhang, *Adv. Funct. Mater.*, 2024, 2401011.
47 S. Li, Y. Liu, K. Feng, C. Li, J. Xu, C. Lu, H. Lin, Y. Feng, D. Ma and J. Zhong, *Angew. Chem., Int. Ed.*, 2023, **62**, e202308670.
48 X. Zhang, Y. Yang, Y. Liu, Z. Jia, Q. Wang, L. Sun, L.-C. Zhang, J. J. Kruzic, J. Lu and B. Shen, *Adv. Mater.*, 2023, **35**, 2303439.
49 Y. Zou, S. A. Kazemi, G. Shi, J. Liu, Y. Yang, N. M. Bedford, K. Fan, Y. Xu, H. Fu, M. Dong, M. Al-Mamun, Y. L. Zhong, H. Yin, Y. Wang, P. Liu and H. Zhao, *EcoMat*, 2023, **5**, e12274.
50 Y. Chen, Q. Li, Y. Lin, J. Liu, J. Pan, J. Hu and X. Xu, *Nat. Commun.*, 2024, **15**, 7278.
51 M. Zhong, M. Xu, S. Ren, W. Li, C. Wang, M. Gao and X. Lu, *Energy Environ. Sci.*, 2024, **17**, 1984–1996.
52 Z. Li, H. Sheng, Y. Lin, H. Hu, H. Sun, Y. Dong, X. Chen, L. Wei, Z. Tian, Q. Chen, J. Su and L. Chen, *Adv. Funct. Mater.*, 2024, **34**, 2409714.
53 S. Venkateswarlu, S. Kim, M. Balamurugan, Y. Son, M. Yoon, K. T. Nam, S. S. Han and M. J. Kim, *Appl. Catal., B*, 2024, **345**, 123609.
54 H. Chen, J. Yu, L. Liu, R.-T. Gao, Z. Gao, Y. Yang, Z. Chen, S. Zhan, X. Liu, X. Zhang, H. Dong, L. Wu and L. Wang, *Adv. Energy Mater.*, 2024, **14**, 2303635.
55 J. Yang, A. R. Mohmad, Y. Wang, R. Fullon, X. Song, F. Zhao, I. Bozkurt, M. Augustin, E. J. G. Santos, H. S. Shin, W. Zhang, D. Voiry, H. Y. Jeong and M. Chhowalla, *Nat. Mater.*, 2019, **18**, 1309–1314.
56 G. Chen, W. Chen, R. Lu, C. Ma, Z. Zhang, Z. Huang, J. Weng, Z. Wang, Y. Han and W. Huang, *J. Am. Chem. Soc.*, 2023, **145**, 22069–22078.
57 Z. Zheng, L. Yu, M. Gao, X. Chen, W. Zhou, C. Ma, L. Wu, J. Zhu, X. Meng, J. Hu, Y. Tu, S. Wu, J. Mao, Z. Tian and D. Deng, *Nat. Commun.*, 2020, **11**, 3315.
58 J. Chen, J. Huang, Y. Zhao, L. Cao, K. Kajiyoshi, Y. Liu, Z. Li and Y. Feng, *Chem. Eng. J.*, 2022, **450**, 138026.
59 C. Zhang, Y. Luo, J. Tan, Q. Yu, F. Yang, Z. Zhang, L. Yang, H.-M. Cheng and B. Liu, *Nat. Commun.*, 2020, **11**, 3724.
60 R. Liu, Z. Gong, J. Liu, J. Dong, J. Liao, H. Liu, H. Huang, J. Liu, M. Yan, K. Huang, H. Gong, J. Zhu, C. Cui, G. Ye and H. Fei, *Adv. Mater.*, 2021, **33**, 2103533.
61 D. Zhang, Z. Wang, X. Wu, Y. Shi, N. Nie, H. Zhao, H. Miao, X. Chen, S. Li, J. Lai and L. Wang, *Small*, 2022, **18**, 2104559.
62 M. Cui, F. Wang, W. Zhao, D. Zhang, R. Liang, Q. Ou and S. Zhang, *Chem. Eng. J.*, 2023, **460**, 141676.
63 S. Parvin, A. Kumar, A. Ghosh and S. Bhattacharyya, *Chem. Sci.*, 2020, **11**, 3893–3902.
64 Q. Yu, Z. Zhang, S. Qiu, Y. Luo, Z. Liu, F. Yang, H. Liu, S. Ge, X. Zou, B. Ding, W. Ren, H.-M. Cheng, C. Sun and B. Liu, *Nat. Commun.*, 2021, **12**, 6051.
65 C. Wang and L. Qi, *Angew. Chem., Int. Ed.*, 2020, **59**, 17219–17224.
66 R. Zhang, Y. Li, X. Zhou, A. Yu, Q. Huang, T. Xu, L. Zhu, P. Peng, S. Song, L. Echegoyen and F.-F. Li, *Nat. Commun.*, 2023, **14**, 2460.
67 L. Wang, Y. Liu, Z. Chen, Q. Dai, C.-L. Dong, B. Yang, Z. Li, X. Hu, L. Lei and Y. Hou, *Nano Energy*, 2023, **115**, 108694.
68 J. Duan, S. Chen, C. A. Ortíz-Ledón, M. Jaroniec and S.-Z. Qiao, *Angew. Chem., Int. Ed.*, 2020, **59**, 8181–8186.
69 X. Xu, K. Guo, J. Sun, X. Yu, X. Miao, W. Lu and L. Jiao, *Adv. Funct. Mater.*, 2024, **34**, 2400397.